Supplementary information

A Measure of Active Interfaces in Supported Catalysts for High-temperature Reactions

Siwon Lee[1, 6]; Hyunwoo Ha[2, 6]; Kyung Taek Bae[3, 6]; Seunghyun Kim[1]; Hyuk Choi[2]; Jun Hyuk Kim[1]; Jongsu Seo[1]; Jin Seok Choi[4]; Yong-Ryun Jo[5]; Bong-Joong Kim[5]; Kang Taek Lee[3, *]; Hyun You Kim[2, *]; WooChul Jung[1, *]

[1]Department of Materials Science and Engineering, Korea Advanced Institute of Science and Technology (KAIST), Daejeon, Republic of Korea

[2]Department of Materials Science and Engineering, Chungnam National University (CNU), Daejeon, Republic of Korea

[3]Department of Mechanical Engineering, Korea Advanced Institute of Science and Technology (KAIST), Daejeon, Republic of Korea

[4]KAIST Analysis center for Research Advancement (KARA), Korea Advanced Institute of Science and Technology (KAIST), Daejeon, Republic of Korea

[5]Department of Materials Science and Engineering, Gwangju Institute of Science and Technology (GIST), Gwangju, Republic of Korea

***Corresponding authors E-mail**: WooChul Jung (wcjung@kaist.ac.kr), Hyun You Kim (kimhy@cnu.ac.kr), Kang Taek Lee (leekt@kaist.ac.kr).

[6]These authors contributed equally: Siwon Lee, Hyunwoo Ha, Kyung Taek Bae.

Fig. S1.

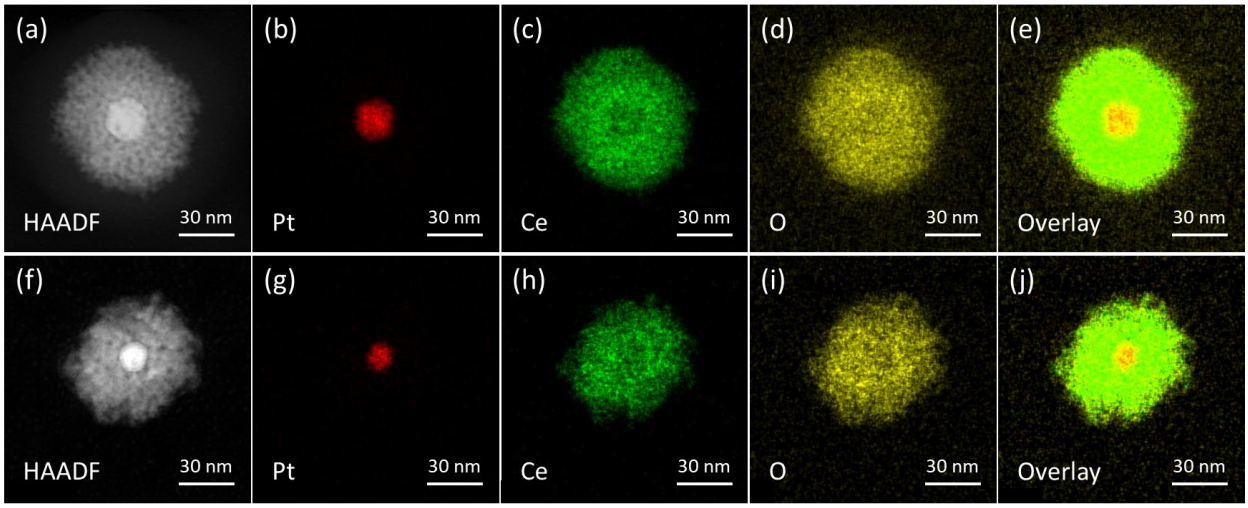

Representative HAADF images and EDS mapping images of (a-e) Pt-large@CeO_2 and (f-j) Pt-small@CeO_2 catalysts

Fig. S2.

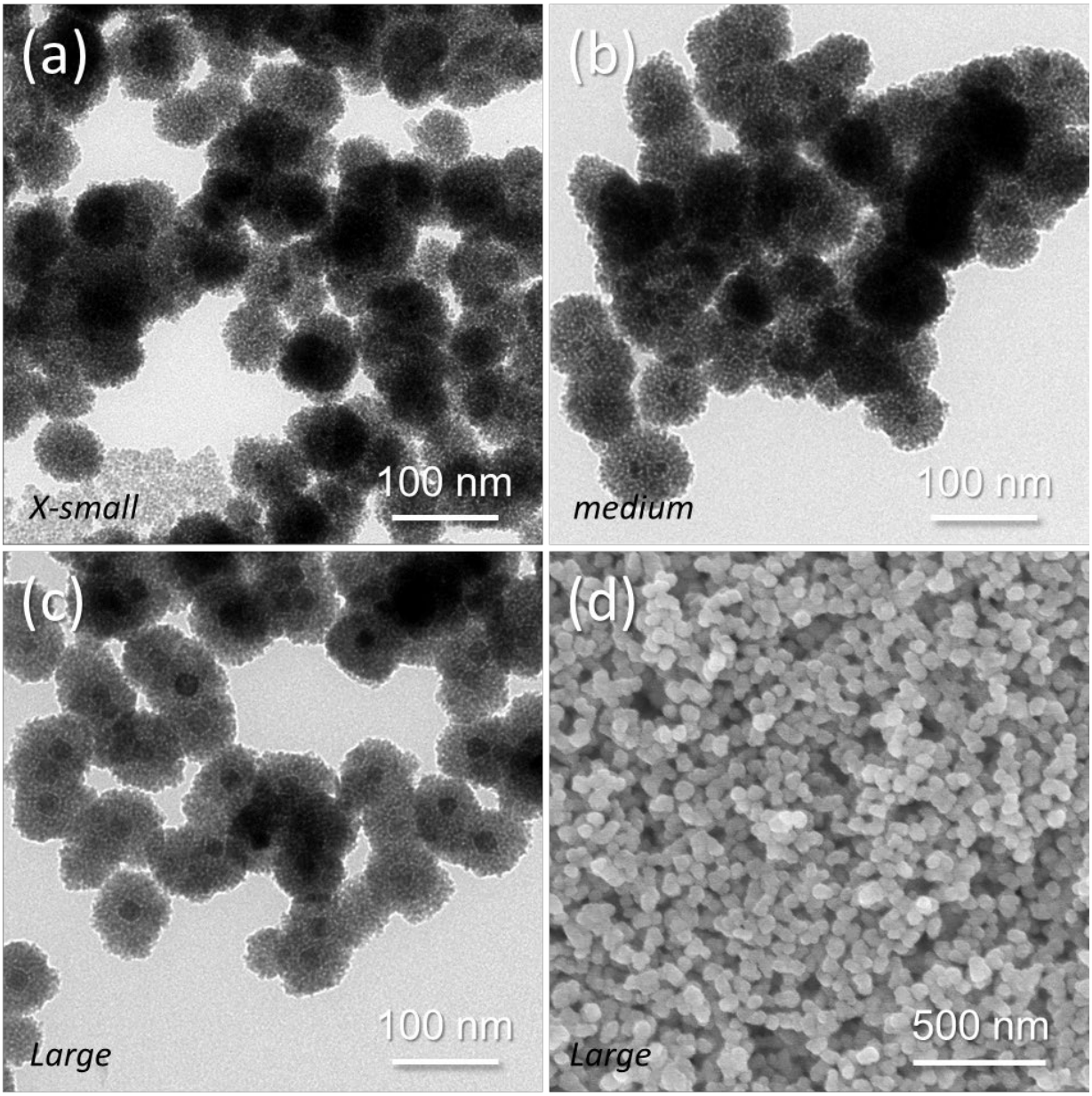

Representative TEM images of Pt@CeO_2 catalysts with (a) x-small Pt NPs, (b) medium-sized Pt NPs, and (c) large Pt NPs. (d) A SEM image of Pt-large@CeO_2 catalysts is also shown.

Fig. S3.

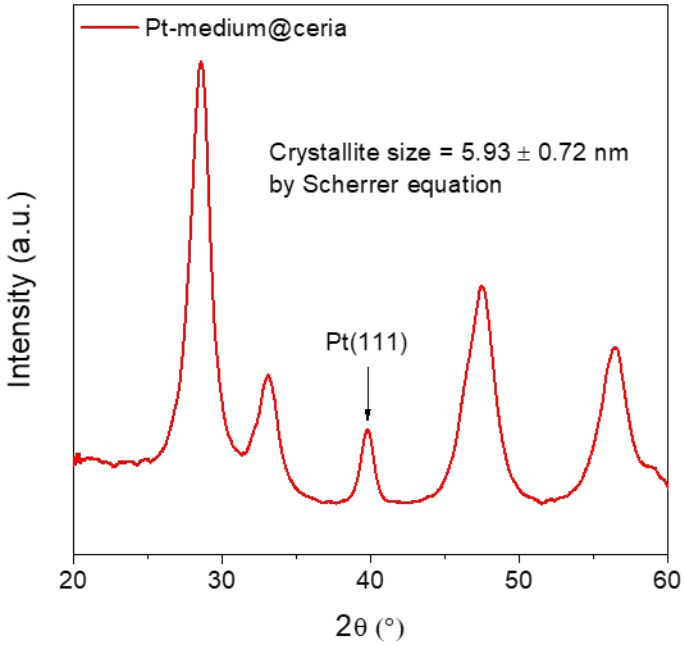

Powder X-ray diffraction (XRD) patterns of Pt-medium@CeO_2. The average crystallite size of CeO_2 in the outer layer was approximately 6 nm, as calculated by the Scherrer equation.

Fig. S4.

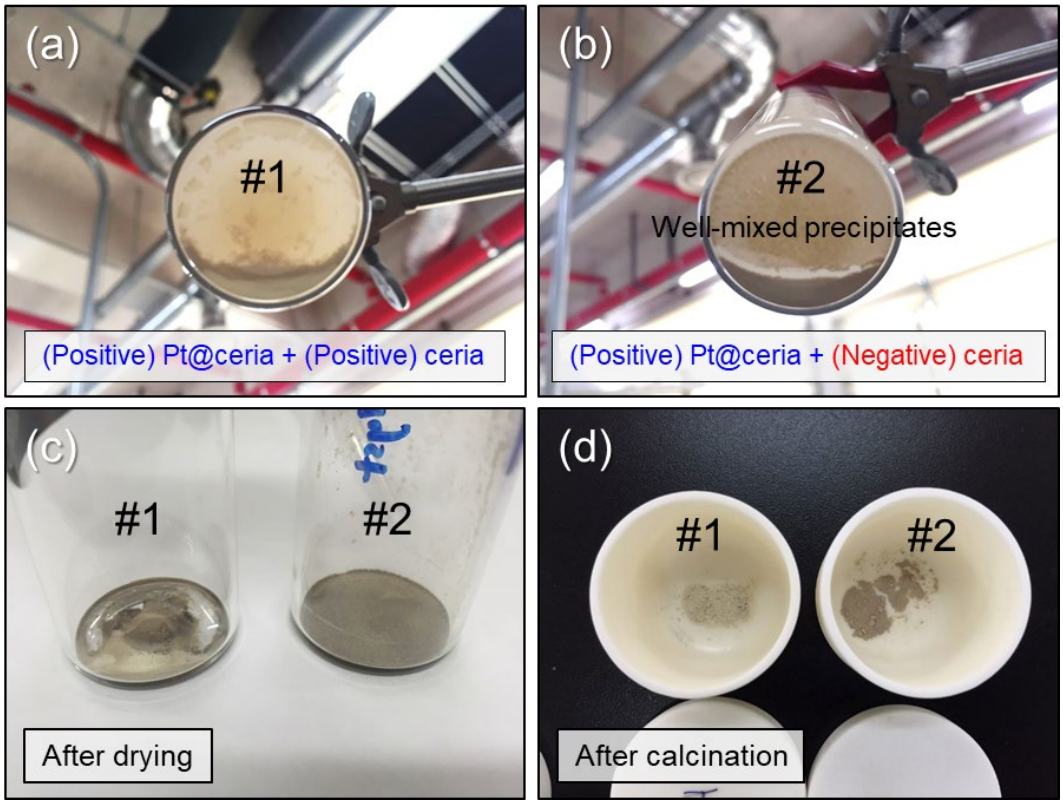

Effect of the surface potential on the resulting Pt@CeO_2/CeO_2 sample: (a) When the surface potential of the CeO_2 support and Pt@CeO_2 are both positive, the Pt@CeO_2 catalyst is not evenly deposited on the CeO_2 support after mixing in a solution (sample #1). On the other hand, (b) when the surface potentials differs from each other between the CeO_2 support and the Pt@CeO_2 catalyst, uniformly mixed precipitates are obtained after mixing in a solution (sample #2). (c, d) The effect of surface potential of the sample can also be confirmed after the drying and calcination steps. The surface potential was measured by a zeta-potential analysis, and these results are compiled in **Table S6**.

Fig. S5.

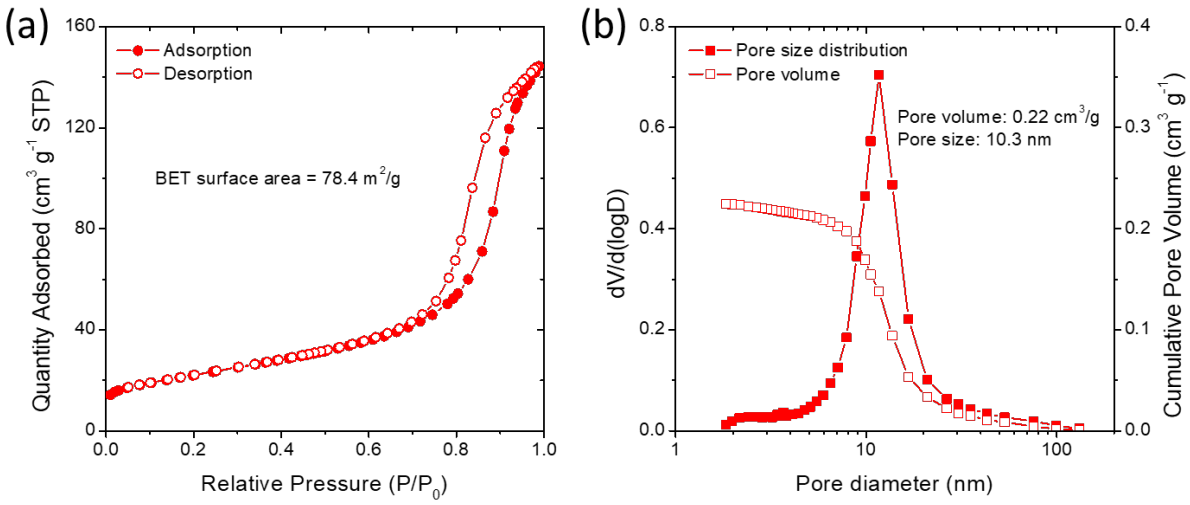

(a) Nitrogen adsorption and desorption isotherms and (b) pore size distribution and cumulative pore volumes for the CeO_2 support. The BET surface area was 78.4 $m^2\ g^{-1}$. The pore volume was 0.22 $cm^3\ g^{-1}$, and the average pore size was 10.3 nm.

Fig. S6.

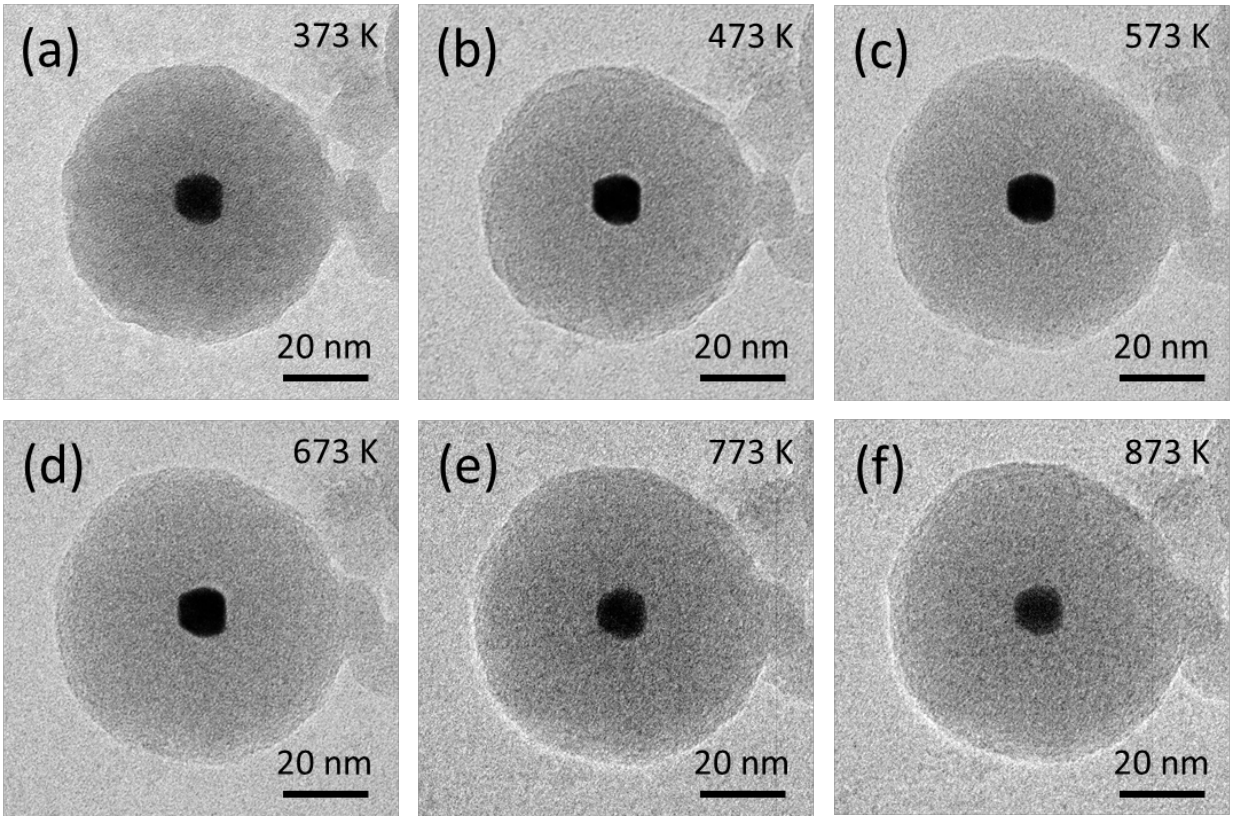

In situ heating TEM observations of Pt-medium@SiO_2 catalysts after heating at (a) 373 K, (b) 473 K, (c) 573 K, (d) 673 K, (e) 773 K, and (f) 873 K.

Fig. S7.

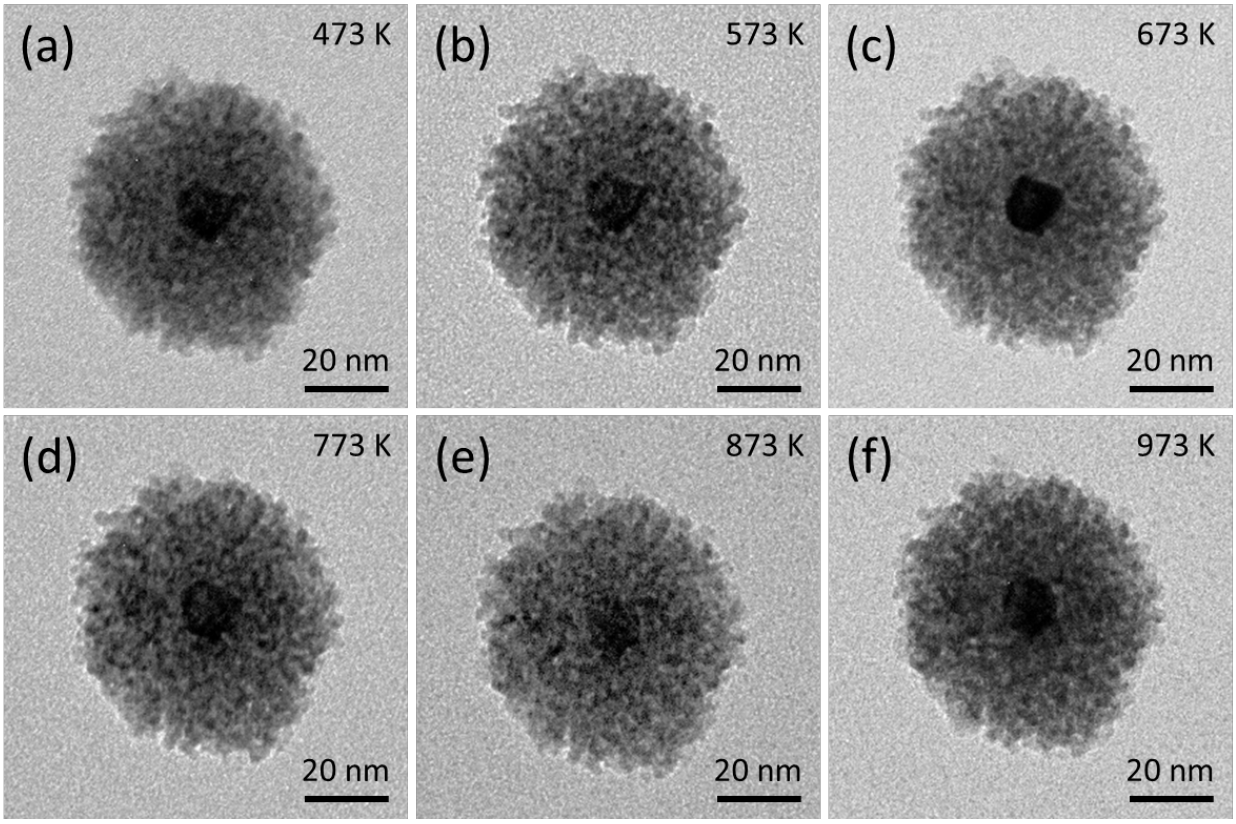

In situ heating TEM observations of Pt-medium@CeO_2 catalysts after heating at (a) 473 K, (b) 573 K, (c) 673 K, (d) 773 K, (e) 873 K, and (f) 973 K.

Fig. S8.

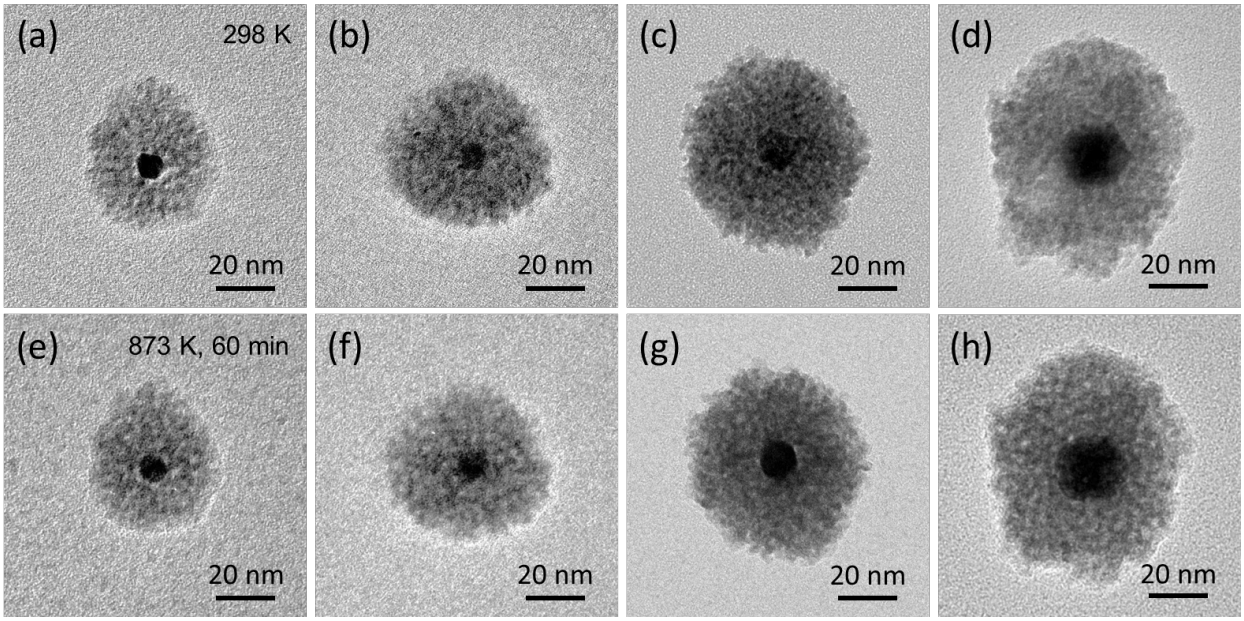

In situ TEM images of CeO_2-encapsulated Pt NPs with different core sizes. The first row shows the morphology of the catalysts at 298 K, and the second row presents the catalysts after annealing at 873 K for 60 min: (a, e) x-small (b, f) small (c, g) medium, and (d, h) large Pt NPs.

Fig. S9.

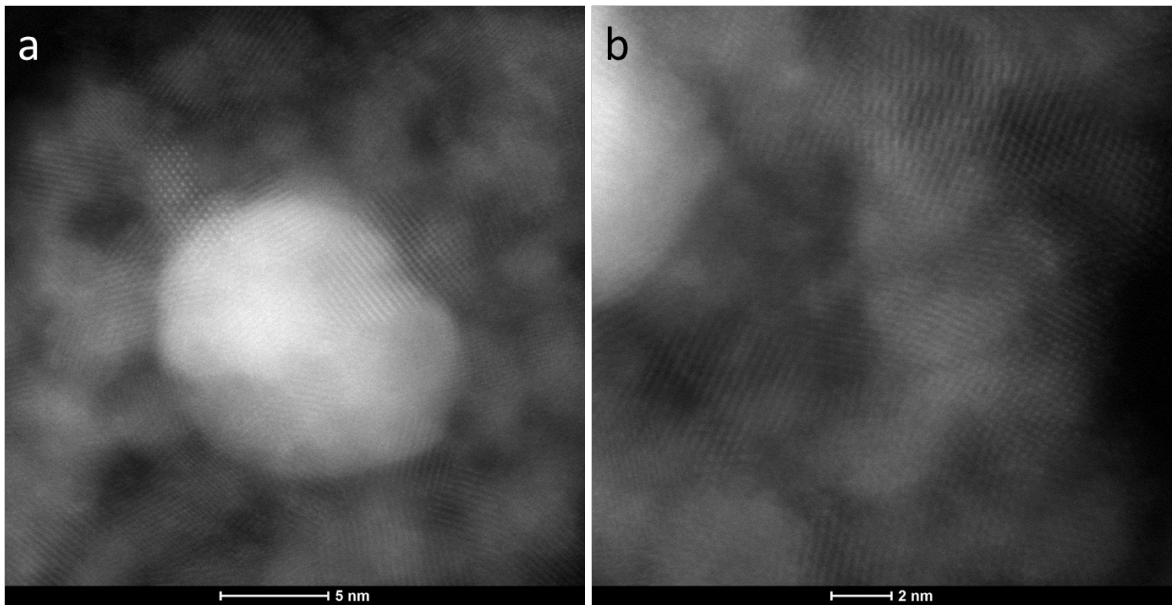

Representative aberration-corrected TEM images of Pt@CeO_2 obtained at (a) 3,600k× and (b) 5,100k× magnification after a thermal treatment at 873 K for 10 h.

Fig. S10.

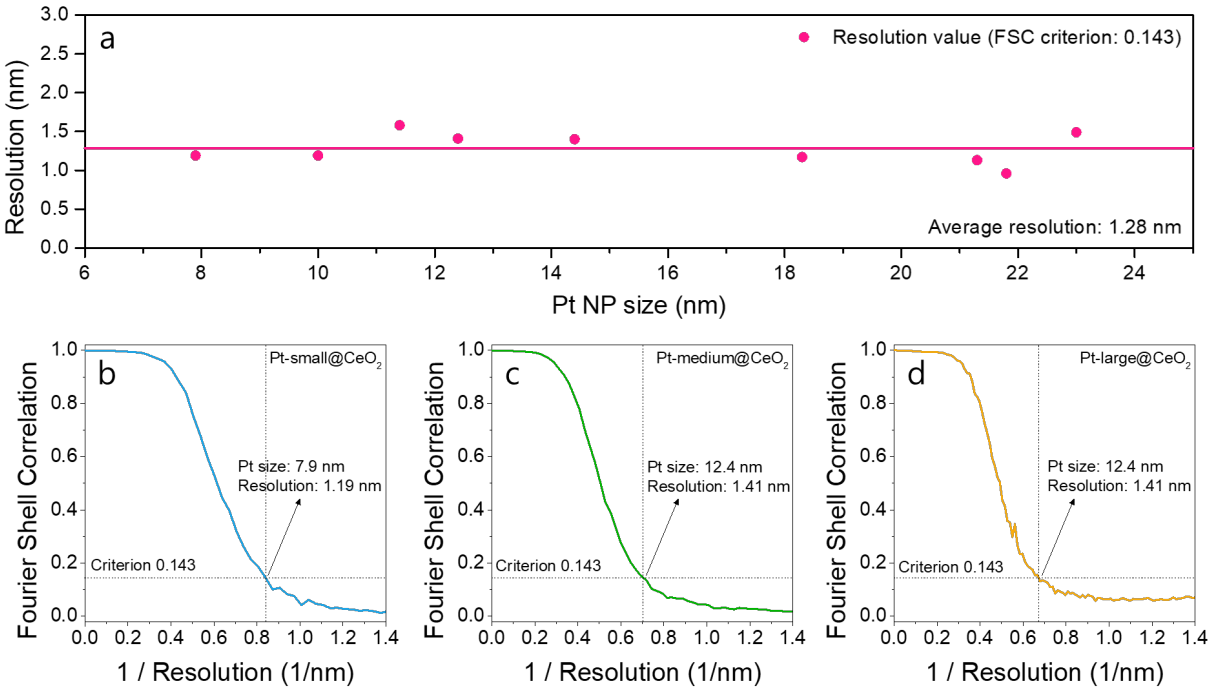

(a) 3D resolution values of samples plotted as a function of the Pt NP size. Representative Fourier shell correlation (FSC) results obtained for the (b) Pt-small@CeO_2, (c) Pt-medium@CeO_2, and (d) Pt-large@CeO_2 samples.

Fig. S11.

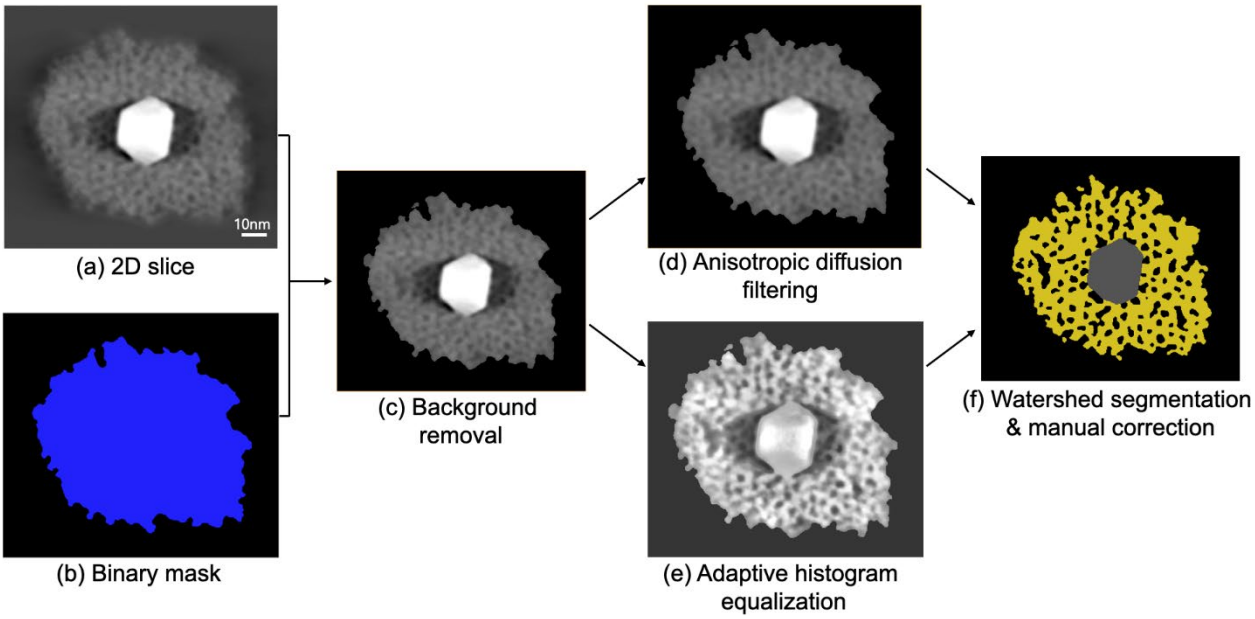

Semi-automated segmentation process applied to tomograms. The background of the original slice of the tomogram was removed by a binary mask (a-c). Anisotropic diffusion filtering (d) and adaptive histogram equalization (e) were performed to reduce the noise and enhance the contrast of each phase, respectively. Designation of each phase (grey: Pt, yellow: ceria, black: pore) was conducted by watershed segmentation and corrected in a manual fashion (f).

Fig. S12.

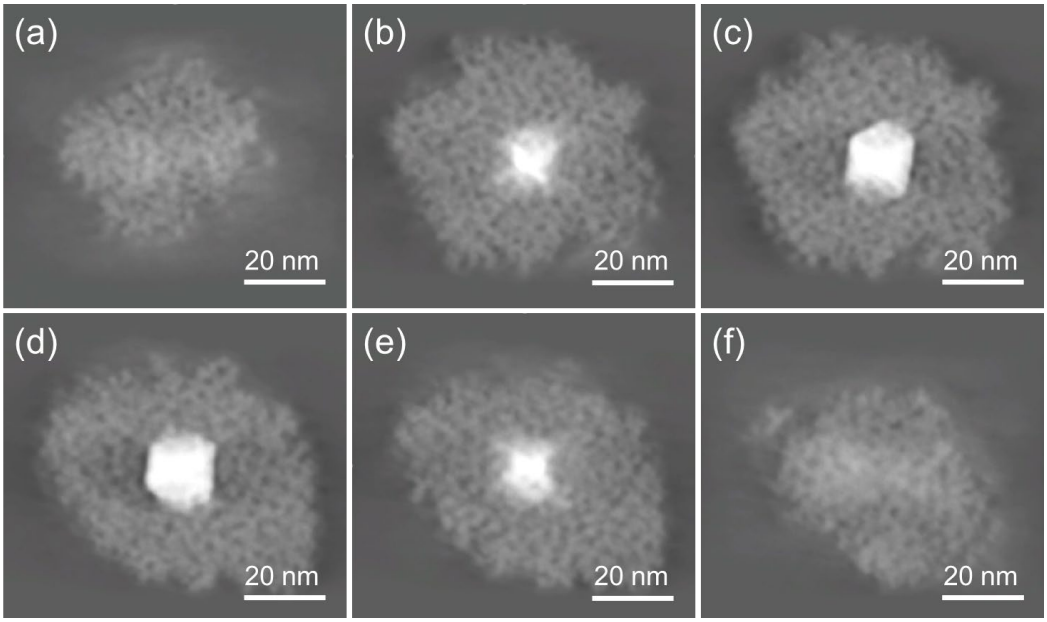

(a to f) Cross-sectional view of the volume-constructed Pt@CeO_2 core-shell catalyst along the Z-axis

Fig. S13.

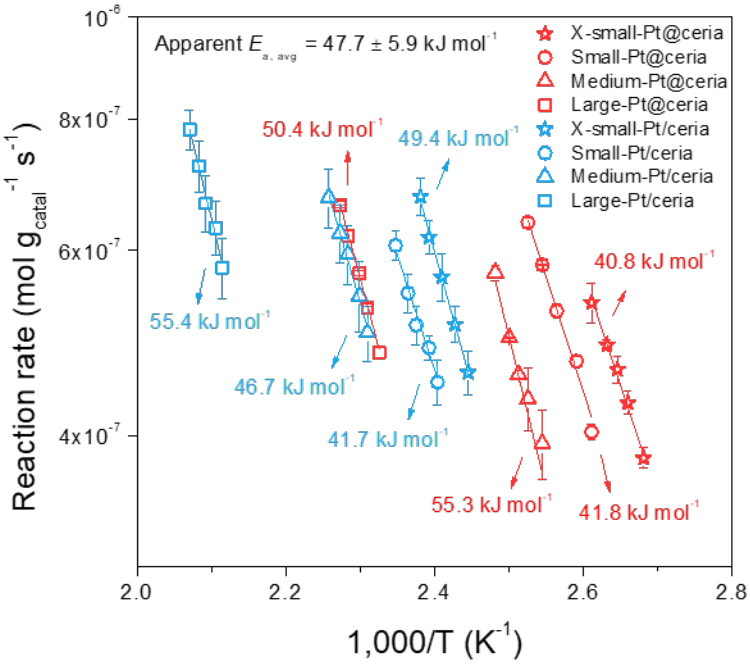

Arrhenius-type plots of CO oxidation over CeO_2-encapsulated (red) and -supported (blue) Pt catalysts. Apparent activation energy values are similar to each other, demonstrating that the reaction mechanism of the Pt-CeO_2 system toward CO oxidation was not affected by the different morphologies of the samples. In addition, the Pt@CeO_2 sample outperforms the CeO_2-supported Pt catalyst regardless of the Pt NP size due to the increased length of the interface in the core-shell structure. Thus, the CO oxidation reaction is mainly governed by the interface between CeO_2 and Pt in Pt@CeO_2. Error bars indicate standard errors for reaction rates.

Fig. S14.

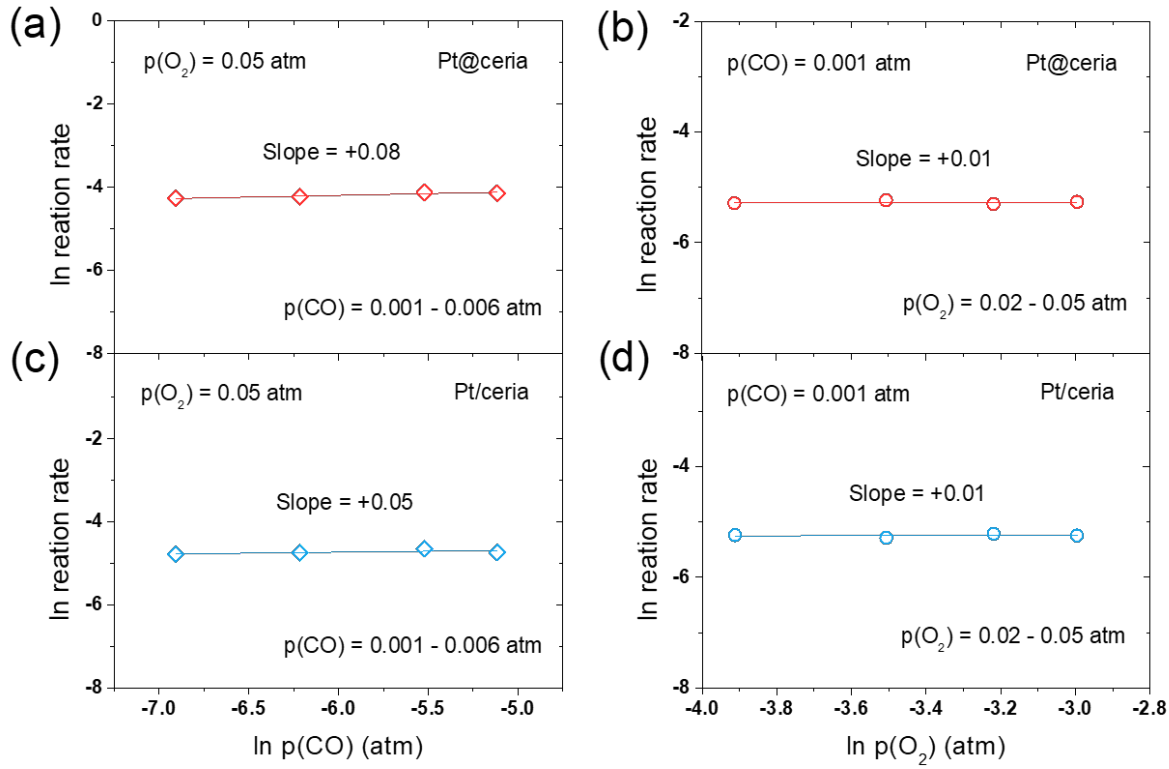

Reaction orders for (a, c) CO and (b, d) O_2 of the Pt-CeO_2 catalysts; top, Pt@CeO_2; bottom; Pt/CeO_2. The reaction orders for CO and O_2 are similar between the Pt@CeO_2 and Pt/CeO_2 catalysts, indicating that the reaction mechanism of Pt-CeO_2 catalysts toward CO oxidation is not affected by the morphology of the catalysts. Thus, the CO oxidation reaction is mainly governed by the interface between CeO_2 and Pt in Pt@CeO_2.

Fig. S15.

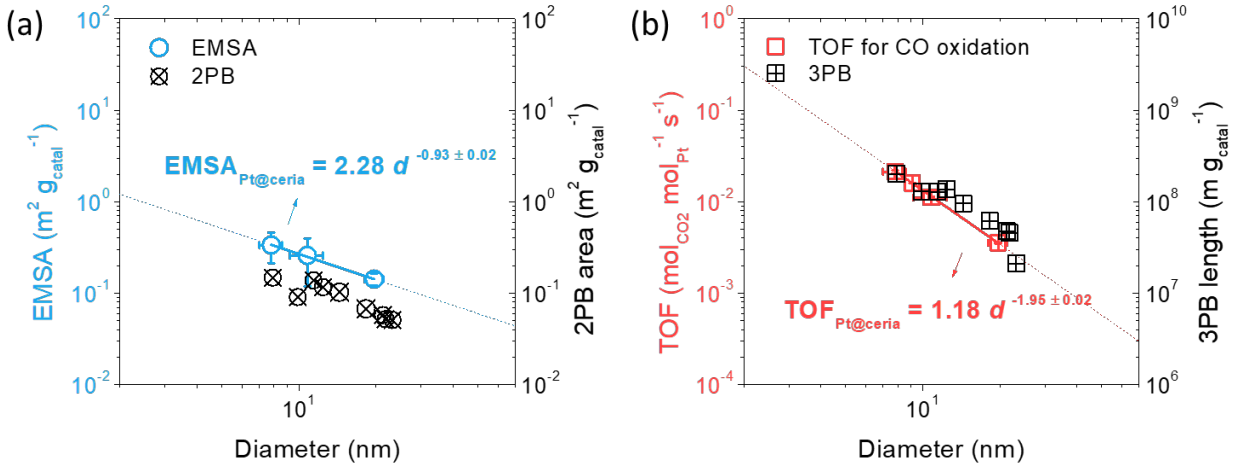

(a) Exposed metallic surface area (blue circle symbols) and (b) TOFs for CO oxidation (red square symbols) at 403 K plotted as a function of the particle diameter of the Pt@CeO_2 catalysts. Circle with superimposed × symbols (⊗) for the 2PB and squared plus symbols (⊞) for the 3PB densities as calculated by 3D tomography are plotted together in (a) and (b), respectively, for reference. These results indicate that the changes of the 2PB and 3PB site density levels determined by CO chemisorption and oxidation experiments according to the diameter are in line with those obtained from 3D electron tomography analyses. Error bars indicate standard errors for particle sizes, EMSA, and TOFs.

Fig. S16.

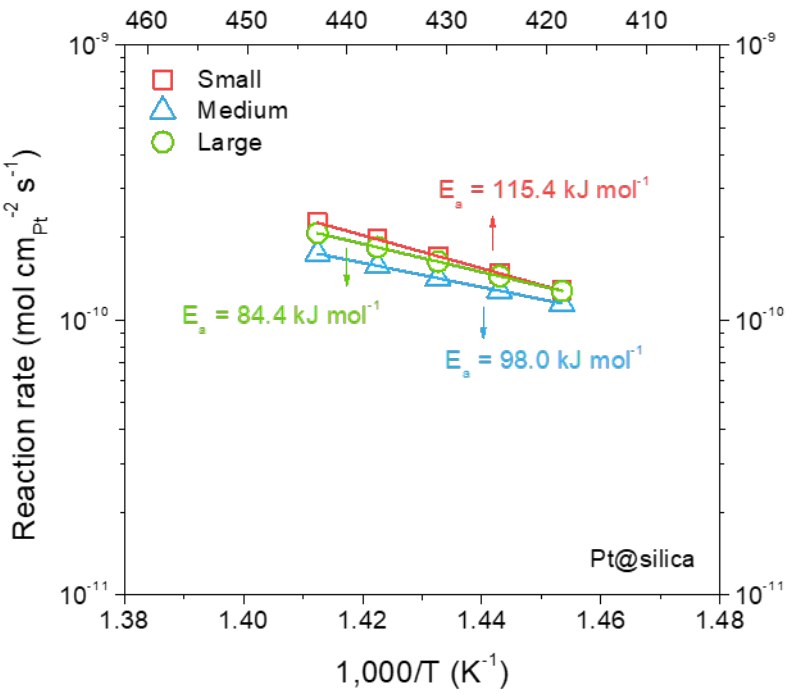

Arrhenius-type plots of CH_4 oxidation over silica-encapsulated Pt catalysts. Reaction rates are normalized according to the exposed metallic surface area, as identified from CO chemisorption analyses. The O_2/CH_4 ratio of the input gas is 4.

Fig. S17.

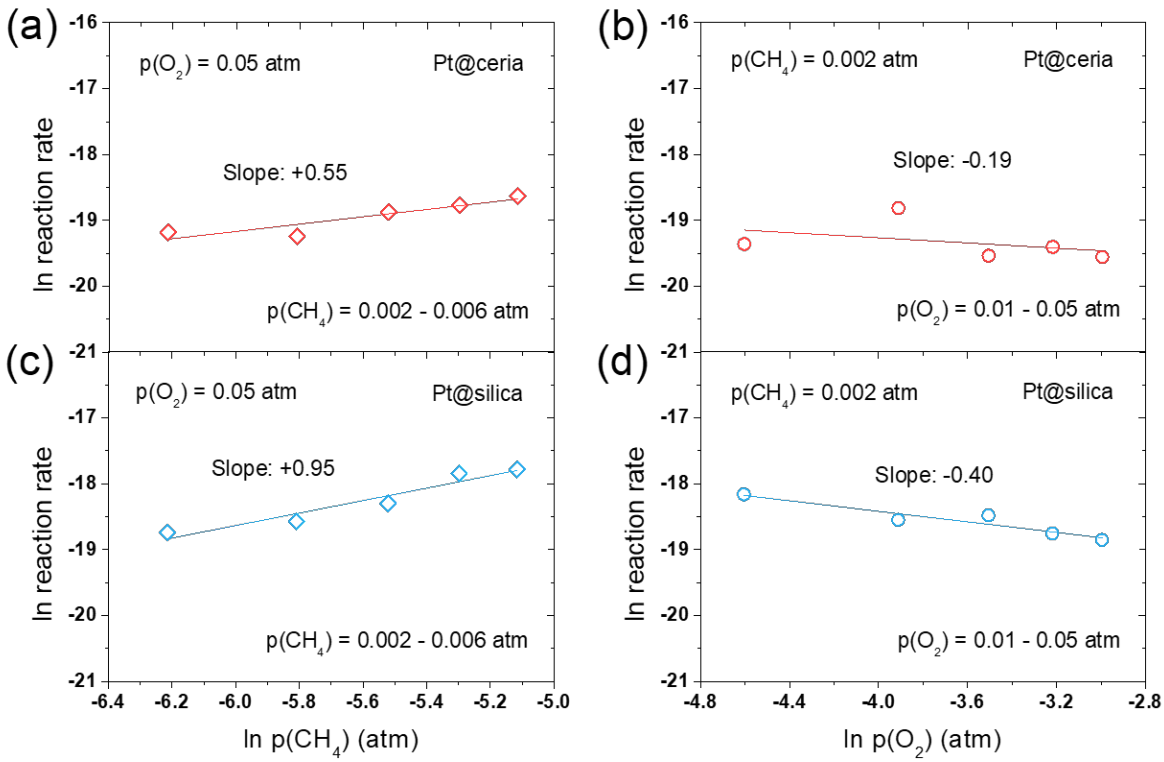

Reaction orders for (a, c) CH_4 and (b, d) O_2 of Pt-CeO_2 and Pt-silica catalysts; top, Pt@CeO_2; bottom; Pt@silica. Reaction orders of Pt@CeO_2 are less dependent on the partial pressure of both CH_4 and O_2 compared to those of Pt@silica, implying the participation of Pt-CeO_2 interface sites towards CH_4 oxidation.

Fig. S18.

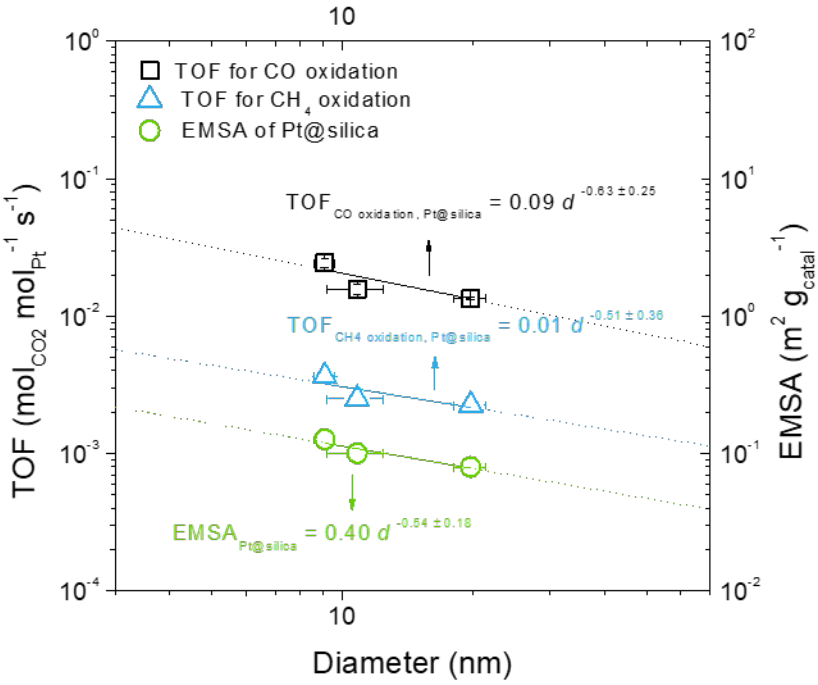

Turnover frequency (TOF) values of CO oxidation at 493 K (black empty squares) and of CH_4 oxidation at 693 K (blue empty triangles) after catalyzation with silica-encapsulated Pt catalysts, and variation in the exposed metallic surface area (EMSA) according to the Pt particle size of Pt@silica (green empty circles). The O_2/CH_4 and O_2/CO ratios of the input gas are both 4. Error bars indicate standard errors for particle sizes.

Fig. S19.

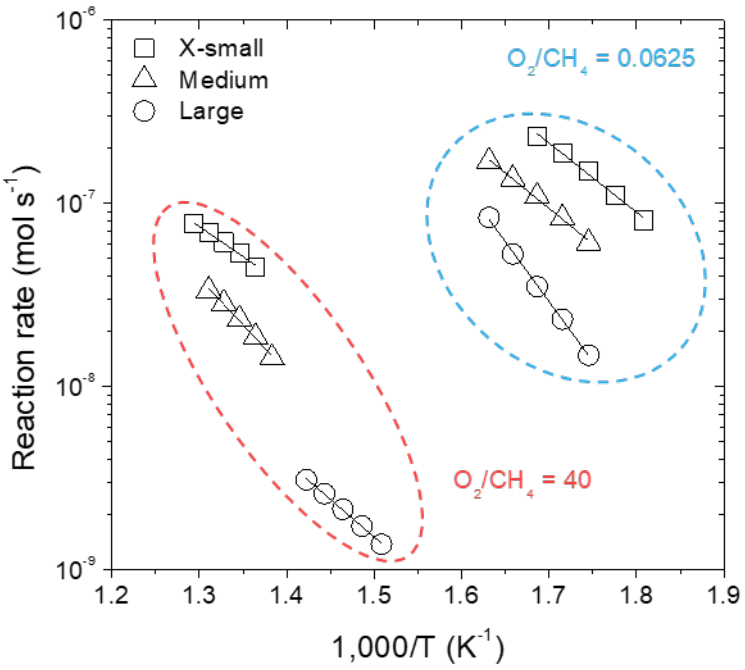

Arrhenius-type plots of CH_4 oxidation over Pt@CeO_2 catalysts. The results were categorized into two groups, as indicated by the red circle (O_2/CH_4 ratio = 40) and the blue circle (O_2/CH_4 ratio = 0.0625). With a higher relative oxygen ratio, more oxygen covers the surface of the Pt, thereby slowing down the overall CH_4 oxidation rate.

Fig. S20.

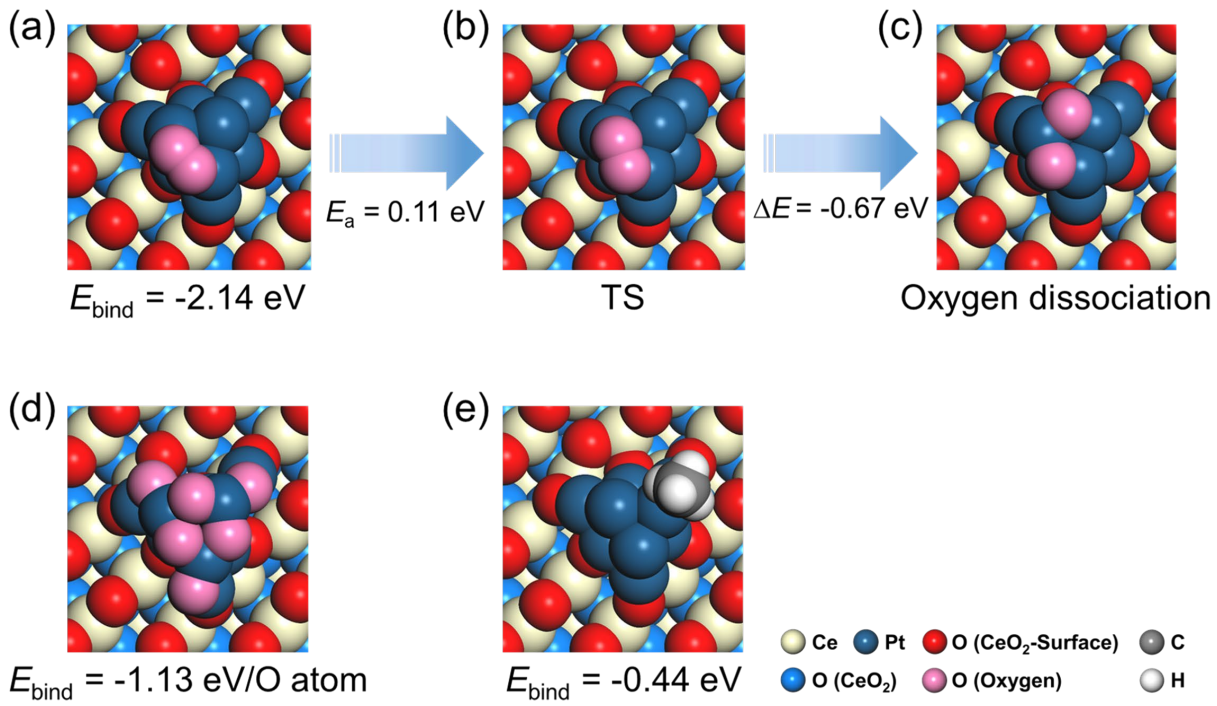

DFT-calculated interaction energy: (a-c) Energetics of O_2 binding and dissociation on a Pt_9/CeO_2 model catalyst, and (d) morphology of the oxygen-saturated Pt/CeO_2 model catalyst. Here, E_{bind} denotes the average binding energy of a single oxygen atom. (e) Binding energy and location of a CH_4 molecule on a Pt/CeO_2 model catalyst.

Fig. S21.

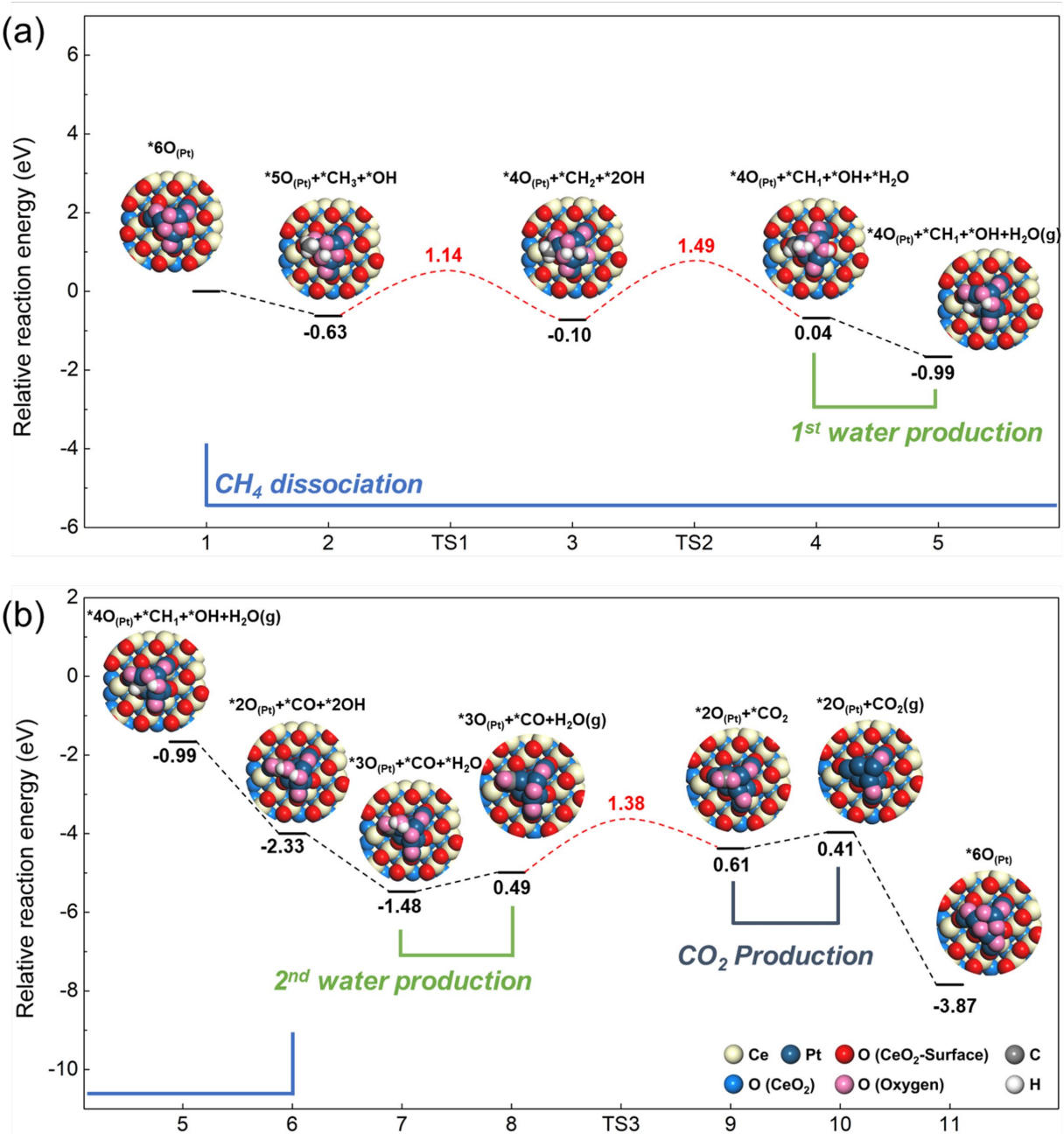

DFT-estimated complete CH_4 oxidation pathway by the 2PB of Pt/CeO_2: (a) energetics of CH_4 binding, CH_4 dissociation, and the first water production; (b) energetics of the second water and CO_2 productions

Fig. S22.

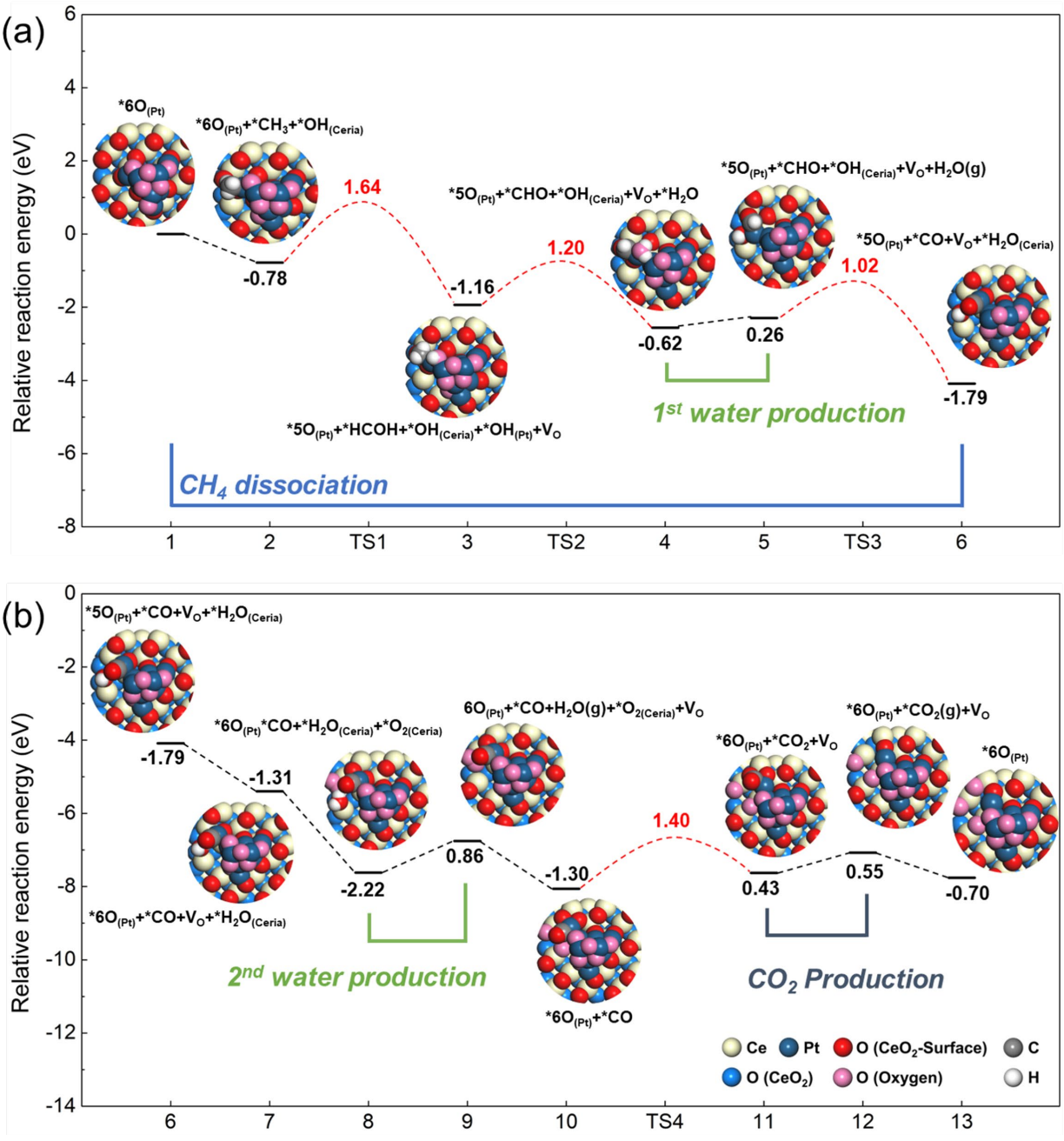

DFT-estimated complete CH_4 oxidation pathway by the 3PB of Pt/CeO_2: (a) energetics of CH_4 binding, CH_4 dissociation, and the first water production; (b) energetics of the second water and CO_2 productions

Fig. S23.

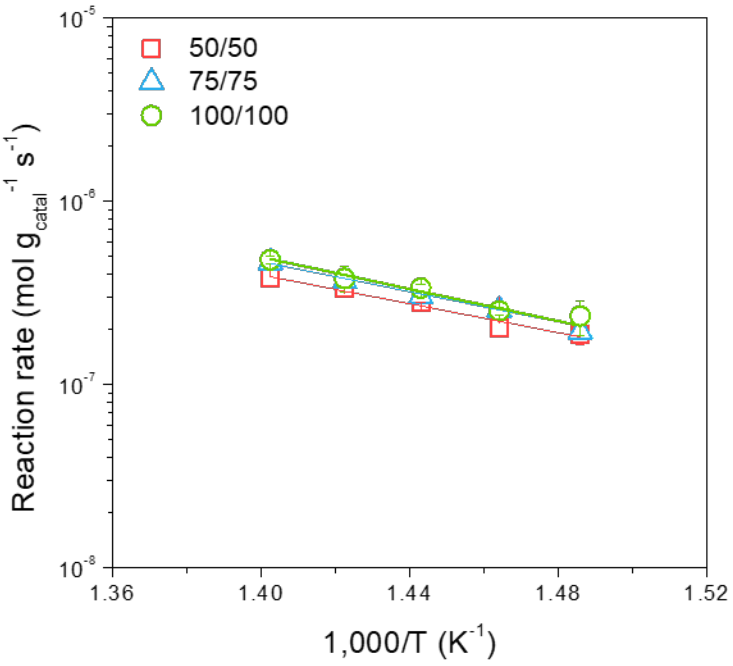

CH_4 oxidation rates of Pt-x-small@CeO_2 catalysts measured when changing the total flow rate at a constant space velocity (60,000 mL g_{catal}^{-1} h^{-1}). The conversion rate remains steady, indicating that neither the mass nor the heat transfer affect the rate of the chemical process. Here, the 50/50 notation refers to the reaction conditions using a 50 mg catalyst and a flow rate of 50 mL min^{-1}. Likewise, the 75/75 and 100/100 notations represent the reaction conditions using, respectively, 75 mg and 100 mg of the catalyst and corresponding flow rates of 75 mL min^{-1} and 100 mL min^{-1}. The O_2/CH_4 ratio of the input gas is 4. Error bars indicate standard errors for reaction rates.

Fig. S24.

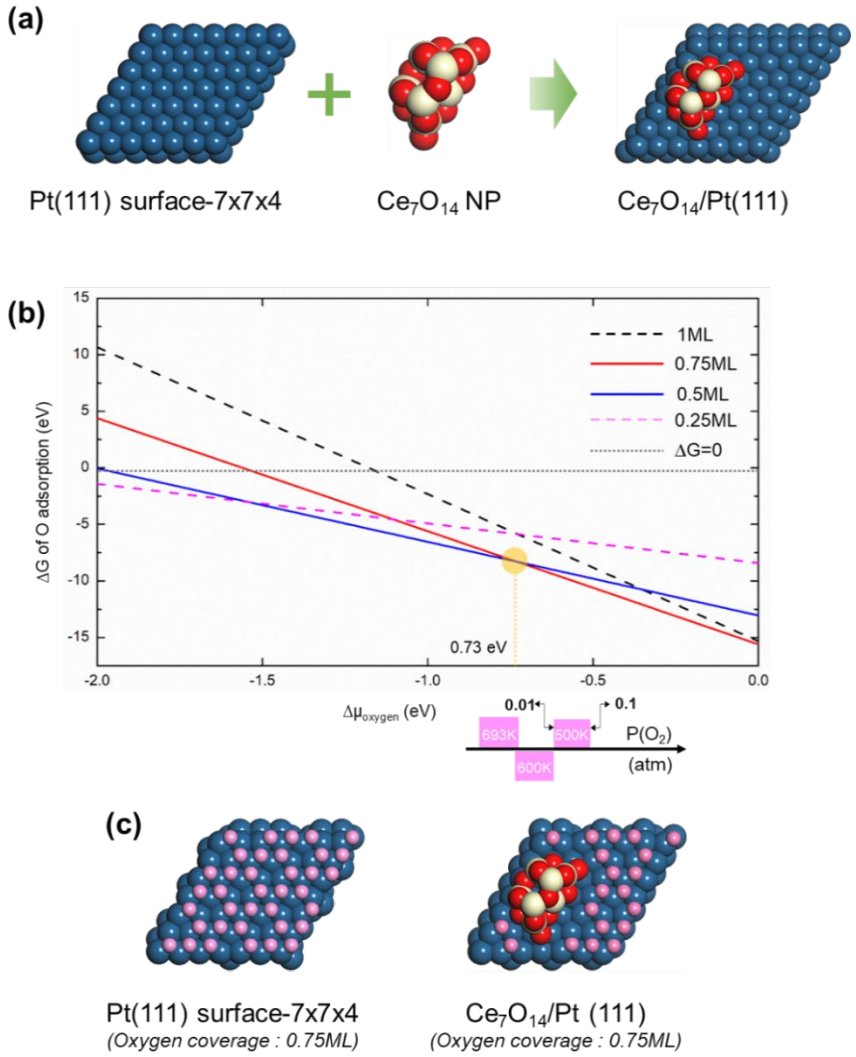

Construction of the inverse Ce_7O_{14}/Pt(111) model used for CH_4 oxidation: (a) Optimized structure models of Pt(111), Ce_7O_{14}, and Ce_7O_{14}/Pt(111). (b) ΔG of oxygen adsorption on Pt(111) presented as a function of the Δμ of oxygen. Individual lines represent Pt(111) covered with the denoted oxygen surface coverage. Details of the ΔG calculation as a function of the Δμ of oxygen can be found in the literature[1]. The yellow vertical line represents the cross point between 0.5ML and 0.75ML. The colored boxes below indicate the range of the oxygen partial pressure (0.01 atm ~ 0.1 atm) at the given temperatures. (c) Optimized Pt(111) and Ce_7O_{14}/Pt(111) with 0.75 ML of oxygen coverage on Pt.

Fig. S25.

(a)

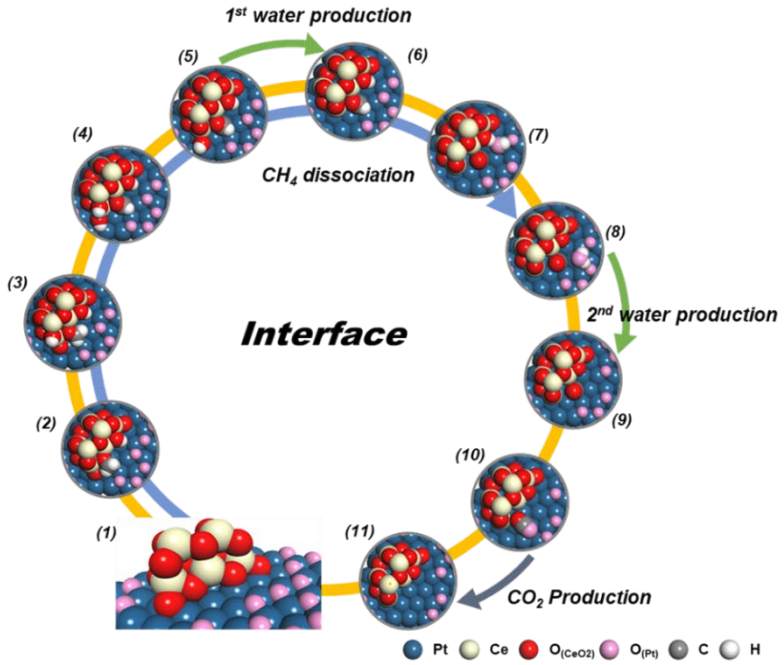

(b)

	Reaction step & Species	Reaction energy(eV)	Activation energy barrier(eV)
(1)	$^*O_{(Pt)}$		
(2)	$^*O_{(Pt)} + ^*CH_3 + ^*OH_{(Ceria)}$	$\Delta E_2 = -1.97$	
(3)	$^*O_{(Pt)} + ^*CH_2 + 2^*OH_{(Ceria)}$	$\Delta E_3 = -1.24$	1.23
(4)	$^*O_{(Pt)} + ^*CH_1 + 3^*OH_{(Ceria)}$	$\Delta E_4 = -1.18$	0.68
(5)	$^*O_{(Pt)} + ^*CH_1 + ^*OH_{(Ceria)} + V_O + ^*H_2O$	$\Delta E_5 = 0.13$	0.93
(6)	$^*O_{(Pt)} + ^*CH_1 + ^*OH_{(Ceria)} + V_O + H_2O(g)$	$\Delta E_6 = 0.88$	
(7)	$^*O_{(Pt)} + ^*CO + ^*OH_{(Ceria)} + ^*OH_{(Pt)} + V_O$	$\Delta E_7 = -0.32$	
(8)	$^*O_{(Pt)} + ^*CO + 2V_O + ^*H_2O$	$\Delta E_8 = -0.29$	
(9)	$^*O_{(Pt)} + ^*CO + 2V_O + H_2O(g)$	$\Delta E_9 = 0.18$	
(10)	$^*O_{(Pt)} + ^*CO_2 + 2V_O$	$\Delta E_{10} = -1.96$	0.52
(11)	$^*O_{(Pt)} + CO_2(g) + 2V_O$	$\Delta E_{11} = 0.59$	

DFT-estimated CH_4 oxidation pathway at the 3PB of Ce_7O_{14}/Pt(111): (a) Sequential process of CH_4 oxidation. (b) Corresponding reaction energy and activation energy barrier of CH_4 oxidation. Here, ΔE_n denotes the reaction energy associated with the reaction from the $(n\text{-}1)^{th}$ state to the $(n)^{th}$ state. The activation energy barrier of the n^{th} state is required to activate the reaction from the $(n\text{-}1)^{th}$ state to the $(n)^{th}$ state.

Fig. S26.

(a)

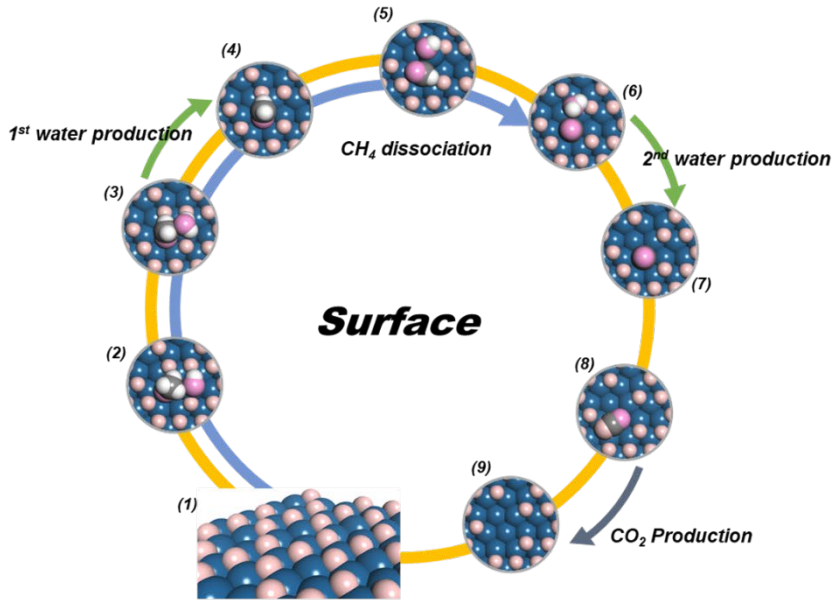

(b)

Pt $O_{(Pt)}$ participated in reaction $O_{(Pt)}$ C H

	Reaction step & Species	Reaction energy(eV)	Activation energy barrier(eV)
(1)	$*O_{(Pt)}$		
(2)	$*O_{(Pt)} + *CH_3 + *OH$	$\Delta E_2 = -1.27$	
(3)	$*O_{(Pt)} + *CH_2 + *H_2O$	$\Delta E_3 = -1.97$	0.22
(4)	$*O_{(Pt)} + *CH_2 + H_2O_{(g)}$	$\Delta E_4 = 0.30$	
(5)	$*O_{(Pt)} + *CH_1 + *OH$	$\Delta E_5 = -1.38$	0.18
(6)	$*O_{(Pt)} + *CO + *H_2O$	$\Delta E_6 = -1.53$	
(7)	$*O_{(Pt)} + *CO + H_2O_{(g)}$	$\Delta E_7 = 0.10$	
(8)	$*O_{(Pt)} + *CO_2$	$\Delta E_8 = -2.06$	0.48
(9)	$*O_{(Pt)} + CO_{2(g)}$	$\Delta E_9 = 0.0$	

DFT-estimated CH_4 oxidation pathway on the 2PB of Ce_7O_{14}/Pt(111): (a) Sequential process of CH_4 oxidation. (b) Corresponding reaction energy and activation energy barrier of CH_4 oxidation. Here, ΔE_n denotes the reaction energy associated with the reaction from the $(n\text{-}1)^{th}$ state to the $(n)^{th}$ state. The activation energy barrier of the n^{th} state is required to activate the reaction from the $(n\text{-}1)^{th}$ state to the $(n)^{th}$ state.

Table S1. The tomography resolution values of the sample used in this study. The resolution was estimated using Fourier shell correlation (FSC) at the criterion of 0.143.

Condition	Pt diameter (nm)	Resolution (nm) <criterion: 0.143>
Before thermal treatment	11.4	1.58
	12.4	1.41
	14.4	1.40
	23.0	1.49
After thermal treatment	7.9	1.19
	10.0	1.19
	18.3	1.17
	21.3	1.13
	21.8	0.96

Table S2. Pt particle size, 2PB area density, and 3PB length density quantified on the basis of the segmentation process. Error bars indicate standard errors for estimated particle size, 2PB area density, and 3PB length density.

Condition	Pt size (nm)	2PB area density (nm^2/g_{Pt})	3PB length density (nm/g_{Pt})
Before thermal treatment	23.2 ± 0.9	$5.0 \times 10^{18} \pm 2.1 \times 10^{17}$	$2.1 \times 10^{18} \pm 8.5 \times 10^{16}$
	14.4 ± 0.3	$1.0 \times 10^{19} \pm 2.4 \times 10^{17}$	$9.5 \times 10^{18} \pm 5.4 \times 10^{17}$
	12.4 ± 0.5	$1.1 \times 10^{19} \pm 4.2 \times 10^{17}$	$1.3 \times 10^{19} \pm 7.8 \times 10^{17}$
	11.4 ± 0.4	$1.3 \times 10^{19} \pm 3.6 \times 10^{17}$	$1.2 \times 10^{19} \pm 7.6 \times 10^{17}$
After thermal treatment	21.8 ± 0.3	$5.1 \times 10^{18} \pm 1.8 \times 10^{17}$	$4.5 \times 10^{18} \pm 2.5 \times 10^{17}$
	21.3 ± 0.4	$5.7 \times 10^{18} \pm 1.4 \times 10^{17}$	$4.7 \times 10^{18} \pm 2.8 \times 10^{17}$
	18.3 ± 0.4	$6.7 \times 10^{18} \pm 2.2 \times 10^{17}$	$6.1 \times 10^{18} \pm 3.5 \times 10^{17}$
	9.9 ± 0.2	$9.0 \times 10^{18} \pm 5.5 \times 10^{17}$	$1.2 \times 10^{19} \pm 6.9 \times 10^{17}$
	7.9 ± 0.1	$1.4 \times 10^{19} \pm 9.2 \times 10^{17}$	$2.0 \times 10^{19} \pm 1.1 \times 10^{18}$

Table S3. Average size of Pt NPs, concentration of Pt NPs dispersed in 5 mL of deionized water, and exposed metallic surface area (EMSA) of Pt@CeO_2 and Pt@silica catalysts as measured by CO chemisorption. Error bars indicate standard errors for particle sizes

Sample	d (nm)	Concentration (ppm)	EMSA (m^2 g^{-1})	
			CeO_2-encapsulated	Silica-encapsulated
Pt-xsmall	7.8 ± 0.8	561.8	0.34	-
Pt-small	9.1 ± 0.5	364.5	-	0.13
Pt-medium	10.8 ± 1.6	707.7	0.26	0.10
Pt-large	19.7 ± 1.7	556.5	0.14	0.08

Table S4. Estimated contribution ratios of the 2PB and 3PB according to the Pt diameter. The reaction temperature is 823 K. The O_2/CH_4 ratio of the input gas is 4.

Pt NP size (nm)	2PB contribution ratio	3PB contribution ratio
1	0.10	0.90
5	0.31	0.69
10	0.45	0.55
20	0.59	0.41
40	0.73	0.27
60	0.79	0.21
80	0.83	0.17
100	0.85	0.15

Table S5. Estimated contribution ratios of 2PB and 3PB according to the Pt diameter. The reaction temperature is 723 K. The O_2/CH_4 ratio of the input gas is 4.

Pt NP size (nm)	2PB contribution ratio	3PB contribution ratio
1	0.02	0.98
5	0.09	0.91
10	0.15	0.85
20	0.25	0.75
40	0.37	0.63
60	0.46	0.54
80	0.52	0.48
100	0.57	0.43

Table S6. Surface potential of pristine CeO_2 and Pt-medium@CeO_2 in the presence/absence of 10 mM of the tetradecyltrimethylammonium bromide (TTAB) surfactant. The potential of deionized water including only TTAB was examined to determine the effect of the TTAB itself on the measured potential. All samples are dispersed in water with a pH value of approximately 10.

Sample	Zeta potential (mV)	
	1st run	2nd run
Pristine CeO_2 [a]	+43.12	+43.14
Pristine CeO_2	-43.36	-45.44
Pt-medium@CeO_2 [a]	+41.66	+40.00
Pt-medium@CeO_2	-49.72	-50.90
Deionized water [a]	-0.40	N/A
Deionized water	-1.56	-1.24

[a] 10 mM of tetradecyltrimethylammonium bromide was added.

Table S7. Representative mass ratios of Pt-medium@CeO_2 and Pt-medium/CeO_2 catalysts as measured by an X-ray fluorescence (XRF) analysis

Sample	Average (mass %)		Standard deviation (mass %)	
	Pt	CeO_2	Pt	CeO_2
Pt-medium@CeO_2/CeO_2	0.91	99.09	0.09	0.09
Pt-medium/CeO_2	1.04	98.96	0.16	0.16

List of Supplementary Video

Video S1. The morphological and mechanical motions of the 3D-reconstructed Pt@CeO_2 core-shell catalysts

Reference

1. Lee J-H, Yoo M, Kang D, Lee H-M, Choi W-h, Park JW*, et al.* Selective SnOx Atomic Layer Deposition Driven by Oxygen Reactants. *ACS Applied Materials & Interfaces* 2018, **10**(39)**:** 33335-33342.